

Analysis of divergent dynamics of exactly factorized electron-nuclear wavefunctions

Julian Stetzler, Sophya Garashchuk, and Vitaly Rassolov*

*Department of Chemistry & Biochemistry,
University of South Carolina, Columbia, South Carolina 29208*

Abstract

The Exact Factorization (XF) of molecular wavefunctions can be viewed as an 'electronic wavepacket' framework for quantum dynamics. It is an appealing alternative to the conventional non-adiabatic dynamics, unfolding in the space of coupled electronic eigenstates. However, implementation of the non-linear XF equations for general systems presents a formidable challenge: the XF counterparts to the non-adiabatic coupling involve division by the nuclear probability density, which leads to severe numerical instabilities in the low-density regions of space. In case of the non-adiabatic dynamics the effect of coupling is relatively smooth, but this theoretical framework becomes impractical when numerous electronic states are involved. In this paper the origin of the XF-specific challenge is analyzed analytically. We demonstrate that the problem arises when the factorized wavefunction diverges, even without the explicit coupling of the Born-Huang electronic states used to describe the molecular wavefunction. Using a 'minimal' model of the photodissociation, we derive expressions for the XF dynamics and locate the source of the XF instability. We analyze the dependence of this instability on the nuclear wavefunction bifurcation in the stationary and moving frames of reference, the latter associated with the quantum trajectory ensemble describing the nuclear XF wavepacket in a compact form. We show that the near-singular behavior persists in the moving frame and in the atomic basis representation of the electronic wavefunction. This model and insight into the root of the XF implementation challenge will help to address the issue, leading to further development of the XF methods.

* rassolov@mailbox.sc.edu

I. INTRODUCTION

A growing number of experiments highlight the nuclear quantum effects on the electron-nuclear dynamics of large molecular systems, including chemical processes in metals and the condensed phase. Some examples include the coupling of electronic excitations to the phonon modes, observed in the vibrational relaxation of CO on Cu or NaCl [1, 2], and the formation of polarons in polarizable materials [3, 4]. For theorists the challenge of describing such processes lies in the failure of the Born-Oppenheimer (BO) approximation, and the inefficiency of the Born-Huang (BH) expansion of molecular wavefunctions requiring computation of many electronic eigenstates [1]. Recent experiments in polaritonic chemistry further motivate the development of theoretical methods for strongly coupled quantum photon-electron-nuclear systems [5]. One such development is the exact factorization (XF) method, introduced to the field of theoretical chemistry in Ref. [6]. The XF is an approach to quantum molecular dynamics based on the product form of time-dependent multi-component wavefunctions, which for clarity of discussion here will be taken as the electron-nuclear wavefunction,

$$\Psi(x, y, t) = \underbrace{\psi(y, t)}_{\text{nuclear}} \underbrace{\Phi(x, y, t)}_{\text{electronic}},$$

subject to the partial normalization condition of Φ in the electronic space its coordinate being x . This condition is defined as $\langle \Phi | \Phi \rangle_x = 1$ for any configuration of the nuclei (coordinate y) at all times, t . Note that, formally, to be 'exact' the electronic component, Φ , is a function of both the electronic and nuclear coordinates. The XF representation is expected to be advantageous for systems involving many electronic states with $\Phi(x, y, t)$ describing an electronic wavepacket, and as a starting point for well-defined approximations to the dynamics of both wavefunction components, necessary for applications to large molecular systems.

Recent conceptual developments include an XF-based theory of electronic friction [7], the factorized electron-nuclear dynamics (FENDy) with a complex potential [8], and extension to polaritonic chemistry [9–11]. Furthermore, the XF ideas were used to develop the approximate Coupled Trajectory-Mixed Quantum Classical (CT-MQC) method [12]. XF-derived decoherence corrections have also been developed for surface hopping and are included in the Libra software package for use with both model and atomistic systems [13].

Thus far, applications of the 'exact' XF were limited to small model systems, such as Tully models [8, 14], 1-dimensional H_2^+ in a laser field with soft coulomb interactions [15, 16], and the Shin-Metiu [17, 18] model where accurate solutions on the full-space can be used. In these studies, XF provided conceptual understanding of molecular Berry phases [19], and the forces driving nuclear dynamics in non-adiabatic systems [20, 21]. Perhaps, the largest chemical application to date is the study of the ring-opening of oxirane, where the approximate CT-MQC method was applied to a realistic molecular system using on-the-fly Density Functional Theory computation of the electronic structure [22–24].

Exact numerical implementation of XF presents a formidable challenge, analyzed in two notable studies: a rigorous mathematical investigation by Lorin [25] and a direct numerical algorithm developed by Gossel and co-workers [26]. These studies mainly attribute the numerical difficulties to the non-classical, also referred to as "quantum", momentum:

$$r(y, t) := \frac{\nabla_y |\psi(y, t)|}{|\psi(y, t)|}.$$

Based on the ongoing research in our group, we argue that the spatial separation of the nuclear wavefunction plays a key role in the numerical stability of the dynamics (Unpublished Observation). As the separation of the diverging wavepackets leads to the near discontinuous steps in the TDPES observed in Ref. [21] and will occur regardless of the non-adiabatic coupling. The nuclear separation has been identified as the cause of these steps [20]. In this work we investigate this regime of dynamics analytically using a simple model which can be used for future method development. The remainder of this paper is organized as follows: Section II presents the model and theoretical background, Section III presents the analytic results and analysis. Section IV concludes.

II. THE FORMALISM AND MODEL

Henceforth we will use the atomic units ($\hbar = 1$) and work with rescaled system parameters defined in Table I. We will refer to the light and heavy particle degrees of freedom (DOFs) as 'electronic' and 'nuclear', and assume the electronic mass of $m = 1$ a.u.; M is the nuclear mass, $M \gg m$. For simplicity of the analysis, we will consider a two-dimensional system using x and y to denote the electronic and nuclear DOFs, respectively. The spatial derivatives will be labeled as gradients, i.e. $\nabla_y = \frac{\partial}{\partial y}$, while $\frac{\partial}{\partial t}$ denotes the partial time-derivative in the stationary, or Eulerian, frame, and $\frac{d}{dt}$ denotes the full time-derivative in the moving, or Lagrangian, frame of reference. The time-dependent parameters are indicated by the subscript t . Integration over x only is denoted $\langle \dots \rangle_x$. Arguments of functions are dropped when unambiguous.

A. Exact factorization of the molecular wavefunction

First, let us summarize the exact factorization (XF) formalism, specifically the factorized electron-nuclear dynamics (FENDy) with complex potential, presented in Ref. [8]. A notable difference between FENDy and the XF framework introduced by Abedi, Maitra and Gross [6], is that the former is based on the complex scalar potential rather than on the vector potential.

Within the XF formalism the electron-nuclear wavefunction $\Psi(x, y, t)$ is represented as a product of the purely *nuclear* component, $\psi(y, t)$, and the *electronic* component, $\Phi(x, y, t)$,

$$\Psi(x, y, t) = \psi(y, t)\Phi(x, y, t), \quad (1)$$

where $\Phi(x, y, t)$ satisfies the partial normalization condition,

$$\langle \Phi | \Phi \rangle_x = 1 \text{ for all } y \text{ and } t. \quad (2)$$

For such representation to be exact, the electronic function formally depends on both x and y . The goal is to have such factorization of the molecular wavefunction, Ψ , that 'most' of the dynamics is captured by $\psi(y, t)$, which will simplify the time-dependence of $\Phi(x, y, t)$ and make it amenable to approximations. Adding and subtracting a complex time-dependent potential energy surface (TDPES) $V_d(y, t)$, the molecular time-dependent Schrödinger equation (TDSE) is separated into the nuclear and electronic equations, respectively:

$$\hat{K}_y\psi + V_d(y, t)\psi = i\frac{\partial\psi}{\partial t}, \quad (3)$$

$$\hat{H}^{BO}\Phi + (\hat{D}_2 + \hat{D}_1)\Phi + \hat{V}_{ext}\Phi - V_d(y, t)\Phi = i\frac{\partial\Phi}{\partial t}. \quad (4)$$

The nuclear TDSE, Eq. (3), does not include any explicit coupling terms, only the nuclear kinetic energy \hat{K}_y and the so-far unspecified complex TDPES, V_d ,

$$V_d(y, t) := V_r(y, t) + iV_i(y, t). \quad (5)$$

In the electronic TDSE (4) \hat{H}^{BO} is the Born-Oppenheimer (BO) Hamiltonian consisting of the electronic kinetic energy and all Coulomb interactions. If present, the external field, e.g. the laser pulse, is included via \hat{V}_{ext} . The TDSE (4) includes the coupling terms, \hat{D}_1 and \hat{D}_2 , containing the derivatives of Φ with respect to the nuclear coordinate,

$$\hat{D}_1 := -\frac{\nabla_y\psi}{\psi}\frac{\nabla_y}{M}, \quad (6)$$

$$\hat{D}_2 := -\frac{\nabla_y^2}{2M}. \quad (7)$$

The derivative coupling operator, \hat{D}_1 , involves the ratio $\nabla_y\psi/\psi$ presenting significant challenges to the numerical implementation of the XF equations.

Within the TDPES of Eq. (5) the purpose of V_r is to minimize the average residual nuclear momentum in Φ , while the role of V_i is to maintain the partial normalization conditions (Eq. (2)). As discussed in Ref. [8], for a system with a *single* nuclear dimension, it is possible to factorize the full wavefunction exactly, such that both the imaginary potential, V_i , and the average residual nuclear momentum, $\langle\Phi|\nabla_y\Phi\rangle$, are equal to zero; the real potential, V_r , driving the evolution of the nuclear wavefunction, $\psi(y, t)$, is defined up to a time-dependent constant. However, in our 'minimal' model, described in Section II C, we will not use V_d or the electronic wavefunction explicitly. We will simply take the electronic wavefunction as an expansion in a basis of N_s eigenstates of the BO Hamiltonian, $\{\phi_i(x, y)\}$,

$$\langle\phi_i|\hat{H}^{BO}|\phi_j\rangle_x = V_{ij}(y), \quad (8)$$

$$\Phi(x, y, t) = \sum_{i=1}^{N_s} C_i(y, t)\phi_i(x, y). \quad (9)$$

Thus, the time-evolution of the electronic wavefunction Φ is described by the complex coefficients, $\{C_i(y, t)\}$, which will be analyzed in terms of their amplitudes and phases as functions of the nuclear position. The dynamics of these coefficients will follow from the properties of the nuclear wavefunction represented in terms of the quantum trajectories reviewed in Section II B.

B. The quantum trajectory formalism

Within the XF formalism, we want the key features of the nuclear dynamics to be captured by $\psi(y, t)$. For an efficient in high-dimensions representation of $\psi(y, t)$, we are considering $\psi(y, t)$ represented as an ensemble of interacting Quantum Trajectories (QT), or Bohmian trajectories, [27]. The QT representation of wavefunctions as a numerical method received the attention of theoretical chemists over the last 25 years (see e.g. Refs [28–32]). The

concept of QTs is also employed for interpretation of the QM phenomena [33, 34], and in a variety of approximate or semiclassical trajectory-based methods. The review of the QT-inspired dynamics is beyond the scope of this work, but to name a few, these methods include dynamics with linearized quantum force [35], quantized Hamiltonian dynamics [36, 37], the QT-surface hopping methods (with and without the XF) [14, 38, 39], and the QT-guided adaptable gaussian bases [40]. There also Bohmian extensions into the phase space [41], multi-polar Bohmian dynamics [42] and stochastic Bohmian mechanics [43]. Formal counterparts to the QT dynamics in non-adiabatic systems have been also proposed (e.g. Refs [44–46]).

In its original form, an ensemble of the QTs, governed by the Newtonian-like equations of motion, is used as a formally exact representation of the wavefunction. The basic formalism is outlined below, and the detailed derivation can be found, for example, in Ref. [28]. The QT formalism hinges on the polar representation of a wavefunction in terms of real phase, S , and amplitude, $|\psi|$,

$$\psi(y, t) := |\psi(y, t)| e^{iS(y, t)}, \quad (10)$$

substituted into the TDSE. The gradient of the wavefunction phase, $P(y, t)$,

$$P(y, t) := \nabla_y S(y, t), \quad (11)$$

is identified as the momentum p_t of a QT at the position y_t ,

$$p_t = P(y, t)|_{y=y_t}. \quad (12)$$

Assuming here a one-dimensional cartesian Hamiltonian, $\hat{H} = -\frac{\nabla_y^2}{2M} + V(y)$, the QT position changes according to the classical equation of motion,

$$\frac{dy_t}{dt} = \frac{p_t}{M}. \quad (13)$$

The particle velocity, p_t/M , defines the Lagrangian frame of reference,

$$\frac{d}{dt} := \frac{\partial}{\partial t} + \frac{p_t}{M} \nabla_y. \quad (14)$$

The remaining QT equations following from the TDSE in the Lagrangian frame are:

$$\frac{dp_t}{dt} = -\nabla_y(V + U)|_{y=y_t} \quad (15)$$

$$\frac{dS_t}{dt} = \frac{p_t^2}{2M} - (V + U)|_{y=y_t}, \quad (16)$$

where U is the quantum potential incorporating quantum-mechanical behavior into otherwise classical equation of the trajectory motion,

$$U(y, t) := -\frac{\hbar^2}{2M} \frac{\nabla_y^2 |\psi|}{|\psi|}. \quad (17)$$

The complementary to Eq. (16) continuity equation for the probability density, $\rho(y, t) = |\psi(y, t)|^2$, leads to the following useful property of the QT dynamics: the weights, $w(y_t)$, of

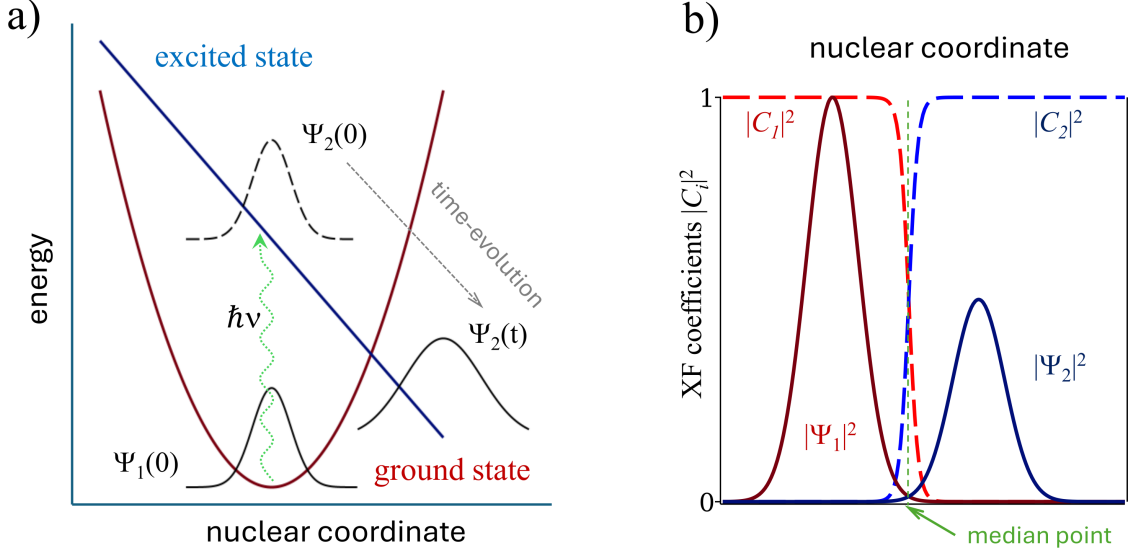


FIG. 1. A minimal model of photodissociation dynamics based on two electronic states. (a) A fraction of the nuclear wavepacket, $\psi_1(0)$, in the ground electronic state (red parabola) is instantaneously transferred into the excited electronic state (blue linear function) of dissociative character. With time this wavepacket, ψ_2 , diverges from ψ_1 in the nuclear coordinate. (b) The probability densities of the Born-Huang nuclear wavepackets ψ_1 (red solid line) and ψ_2 (blue solid line) add up to the XF nuclear wavefunction, $|\psi|^2 = \sum_i |\psi_i|^2$, defining the expansion amplitudes, $|C_1|$ (red dash) and $|C_2|$ (blue dash) of the XF complement to ψ in the electron-nuclear space. For diverging wavepackets, $|C_i|$ behave as step-functions near the median point of equal $|\psi_i|^2$ values.

QT trajectories, defined as the probability density within the volume element dy_t associated with the trajectory (y_t, p_t) ,

$$w(y_t) = |\psi(y_t)|^2 dy_t. \quad (18)$$

are constant in time [47]. In one nuclear dimension this property allows one to generate the QT position from the probability density of the full wavefunction by simply finding y_t for a fixed value of the cumulative density, ρ_c , at every moment of time,

$$\rho_c(y_t) = \int_{-\infty}^{y_t} |\psi(y, t)|^2 dy = \int_{-\infty}^{y_t} \int_{-\infty}^{\infty} |\Psi(x, y, t)|^2 dx dy. \quad (19)$$

In Eq. (19) the second equality applies for the XF wavefunction given the conditional normalization of Eq. (2). Eq. (19) is used to generate QTs numerically. Additional discussion and examples of the QT dynamics on a single BO surface and within the XF formalism applied to a two-state system can be found in Appendix A.

C. The model

Our basic model of photodissociation, sketched in Fig. 1(a), consists of the nucleus of mass M described by the coordinate y , evolving on two electronic states, $N_s = 2$. We assume that a certain fraction of the nuclear wavepacket was instantaneously transferred from the ground electronic state, $|\phi_1\rangle$, to the excited electronic state, $|\phi_2\rangle$. The electronic states are assumed to be orthonormal.

XF nuclear wavefunction $\psi(y, t)$		
A	phase: $S := \arg(\psi)$	momentum: $P := \nabla_y S$
Born-Huang nuclear wavefunction $\psi_i(y, t)$		
B	phase: $S_i := \arg(\psi_i)$	momentum: $p_i := \nabla_y S_i$
transformation a.u. \rightarrow scaled units		
C	$\alpha_{coh} := M\omega$ (a.u.)	$\sqrt{\alpha_{coh}}y \rightarrow y$
D	$\alpha_t/\alpha_{coh} \rightarrow \alpha_t$	$\beta_t/\alpha_{coh} \rightarrow \beta_t$
		$\bar{p}_t/\sqrt{\alpha_{coh}} \rightarrow \bar{p}_t$

TABLE I. The model parameters and definitions. Rows A and B define quantities of the nuclear wavefunctions. Rows C and D define transformation from the atomic units to scaled units.

In the ground electronic state, the nuclear subsystem is described by a harmonic oscillator with the frequency ω . For the excited electronic state, the potential is a linear function of y . The electronic states are uncoupled, i. e. in Eq. (8) $V_{12} = 0$. Shifting the potentials by $-\omega/2$ to reduce the time-dependence of the nuclear wavefunction in the ground state, the Born-Oppenheimer Hamiltonian matrix in atomic units becomes:

$$\mathbf{H}^{BO} := \begin{bmatrix} \frac{M\omega^2}{2}y^2 - \frac{\omega}{2} & 0 \\ 0 & -ky - \frac{\omega}{2} \end{bmatrix}. \quad (20)$$

This model allows us to study the behavior of the XF electronic expansion coefficients $C_i(y, t)$ during the nuclear dynamics without explicit functional form of the electronic functions.

To streamline the analysis, the nuclear wavepacket $\psi_1(y, 0)$ on the ground electronic surface is taken as the vibrational ground state of $V_{11} = (M\omega^2y^2 - \omega)/2$, its width parameter equal to the coherent value, α_{coh} , $\alpha_{coh} = M\omega$,

$$\psi_1(y, t) := \sqrt{1-\lambda^2} \left(\frac{\alpha_{coh}}{\pi} \right)^{1/4} \exp \left(-\frac{\alpha_{coh}y^2}{2} \right). \quad (21)$$

In the absence of coupling the wavepacket ψ_1 is time-independent.

We assume that at $t = 0$, the laser pulse creates a Gaussian wavepacket ψ_2 in the excited electronic state with population of λ^2 ,

$$\psi_2(y, t) := \lambda \left(\frac{\alpha_t}{\pi} \right)^{1/4} \exp \left(-\frac{\alpha_t + i\beta_t}{2}(y - q_t)^2 + i\bar{p}_t(y - q_t) + i\gamma_t \right). \quad (22)$$

For $V_{22} = -ky - \omega/2$, ψ_2 depends on time through its parameters as follows:

$$\bar{p}_t = \bar{p}_0 + kt, \quad q_t = q_0 + \frac{\bar{p}_0}{M}t + \frac{k}{2M}t^2 \quad (23)$$

$$\alpha_t = \frac{\alpha_0}{1 + \tau^2}, \quad \beta_t = \beta_0 - \frac{\alpha_0\tau}{1 + \tau^2}, \quad \text{where } \tau := \frac{\alpha_0 t}{M} \quad (24)$$

$$\gamma_t = \gamma_0 + kq_0t + \frac{t}{M} \left(\frac{k^2t^2}{3} + k\bar{p}_0t + \frac{\bar{p}_0^2}{2} \right) + \frac{\omega t - \arctan \tau}{2}. \quad (25)$$

Henceforth, we will use the *scaled variables and parameters* of the wavefunctions, defined in Table I, without introducing new notations. In the scaled variables $\alpha_{coh} = 1$.

D. Definition of the XF electronic coefficients

The XF electronic coefficients C_i ($i = 1, 2$) in Eq. (9) are obtained by equating the XF wavefunction given by Eqs (1) and (9) to the usual Born-Huang (BH) expansion:

$$\Psi(x, y, t) = \psi(y, t) \sum_{i=1,2} C_i(y, t) \phi_i(x, y) = \sum_{i=1,2} \psi_i(y, t) \phi_i(x, y). \quad (26)$$

This is equivalent to the procedure of Ref. [48], where the XF solution is derived from the eigenvectors of the density matrix yielding

$$C_i = \frac{\psi_i}{\psi}. \quad (27)$$

The XF coefficients will be analyzed in terms of their real moduli, $|C_i|$, and phases, θ_i ,

$$C_i = |C_i| \exp(i\theta_i). \quad (28)$$

Since Φ satisfies the partial normalization condition of Eq. (2), the XF nuclear probability density is equal to

$$|\psi|^2 = |\psi_1|^2 + |\psi_2|^2, \quad (29)$$

and given that $\{\phi_i(x, y)\}$ are orthonormal for each y , $|C_i|^2$ are:

$$|C_i|^2 = \frac{|\psi_i|^2}{|\psi_1|^2 + |\psi_2|^2}. \quad (30)$$

From Eq. (30) it is already clear that as the nuclear BH wavepackets diverge, $\langle |\psi_1| \mid |\psi_2| \rangle \rightarrow 0$, the amplitudes $|C_i|$ become either 0 or 1. As discussed in Ref. [21] and illustrated in Fig. 1(b), the amplitudes $|C_i|$ behave as step-functions near the point of equal probability density associated with the two electronic states. The step-functions are also present in the phases of the XF coefficients, θ_i , defined as the difference of the phases of ψ_i (the nuclear wavepackets in the BH representation of Eq. (26)) and the phase S of the nuclear XF function, $\psi(y, t)$, $S(y, t) := \arg(\psi(y, t))$. In *one nuclear dimension* the latter is obtained (up to a constant) as the integral of its gradient, $P(y, t) := \nabla_y S(y, t)$, which matches the QT definitions of Eqs (10) and (11). Within the XF framework $P(y, t)$ is uniquely defined as the x -averaged nuclear momentum of the full wavefunction Ψ :

$$P(y, t) = \Im \left(\frac{\langle \Psi | \nabla_y | \Psi \rangle_x}{\langle \Psi | \Psi \rangle_x} \right) = \frac{p_1 |\psi_1|^2 + p_2 |\psi_2|^2}{|\psi_1|^2 + |\psi_2|^2}, \quad (31)$$

where $\{p_i\}$ denote the momentum of each BH wavepacket,

$$p_i(y, t) := \Im \left(\frac{\nabla_y \psi_i}{\psi_i} \right). \quad (32)$$

Then, the phases, θ_i , of the XF coefficients C_i are

$$\theta_i(y, t) = \arg(\psi_i(y, t)) - S(y, t). \quad (33)$$

Model parameters (scaled units)					
$M = 1$	$\omega = 1$	$k = 2$	$V_1(0) = -\frac{1}{2}$	$V_2(0) = -\frac{1}{2}$	
Wavefunction parameters (scaled units)					
$\alpha_0 = 1$	$\beta_0 = 0$	$q_0 = 0$	$\bar{p}_0 = 0$	$\gamma_0 = 0$	$\lambda = 1/\sqrt{3}$

TABLE II. Parameters of the model and initial wavefunction used in the analysis unless stated otherwise.

III. RESULTS AND DISCUSSION

In this Section we argue that the step-function character of the electronic coefficients underlies the challenges of the numerical implementation of the XF-type methods. Unless specified otherwise, the model and the initial wavefunction parameters given in Table II are used in the analysis.

The time-evolution equations are obtained from the TDSE (4) for the XF coefficients in polar form of Eq. (28). Using the derivative operators, defined in Eqs (6, 7), the formal EOMs in the stationary frame are:

$$\frac{\partial|C_i|}{\partial t} = \Im\left(e^{-i\theta_i}((\hat{D}_1 + \hat{D}_2)C_i)\right) - V_i|C_i| \quad (34)$$

$$\frac{\partial\theta_i}{\partial t} = -\Re\left(C_i^{-1}((\hat{D}_2 + \hat{D}_2)C_i)\right) + V_r - H_{ii}^{BO}. \quad (35)$$

In the moving frame defined by a QT, $\dot{y}_t = p_t/M$ (Eq. (14)), the counterpart to Eq. (34) becomes

$$\frac{d|C_i|}{dt} = \frac{\partial|C_i|}{\partial t} + \frac{p_t}{M} \nabla_y |C_i|, \quad (36)$$

with the last RHS term canceling part of the term containing $\hat{D}_1 C_i$, and likewise for $d\theta_i/dt$. However, for simplicity we will use the explicit form of $|C_1(t)|$ from Eqs (21, 22) and (30). As follows from Eq. (30) time-dependence of $|C_2(t)|$ is complementary to that of $|C_1(t)|$. As noted previously in the one-dimensional case, V_r can be chosen such that $V_i = 0$.

We will analyze the behavior of $C_1(y, t)$ near the point of the largest change in the populations, i.e near the point of equal density between the centers of ψ_1 and ψ_2 , which will henceforth be referred to as the median, $y_m(t)$

$$|\psi_1(y, t)|_{y=y_m} = |\psi_2(y, t)|_{y=y_m}. \quad (37)$$

The initial wavefunction ψ_2 is defined as $\alpha_0 = 1, \beta_0 = 0, q_0 = 0, \bar{p}_0 = 0$ (Table II). Equations (34) and (36) are examined assuming the 'frozen' wavepacket approximation for ψ_2 , $\alpha_t = 1$, or in other words in the limit of small τ in Eqs (24). This approximation removes the spreading of the QTs, which simplifies the analysis of the electronic coefficient behavior; while preserving the essential features of the dynamics as shown next.

The QT positions, y_t , obtained from the evolution of the exact and frozen wavepackets are displayed in Fig. 2(a,c). The centers of ψ_2 and ψ_1 (the latter equal to zero for all t), and y_m are shown as red dash and as green dot-dash, respectively. Comparing these two panels, we see that y_m moves at a faster rate in the case of frozen ψ_2 ($\alpha_t = 1$), but follows the same

trend as the exact y_m . In the frozen case y_m is equal to

$$y_m = \frac{q_t}{2} + \frac{\ln(\eta)}{2q_t}, \quad (38)$$

where η denotes the ratio of the full populations of the two electronic states,

$$\eta := \frac{1 - \lambda^2}{\lambda^2}. \quad (39)$$

The moduli of the corresponding electronic coefficients, $|C_1(y_t)|$, are displayed in Fig. 2(b,d). We observe that the frozen wavepacket approximation does not change the qualitative dependence of $|C_1|$, and that the largest changes in the state populations of QTs, $|C_1(y_t)|^2$, indeed, occur near $y_t = y_m$, marked with the open circles.

To analyze the effect of the moving frame on the behavior of C_i let us compare Eqs (34) and (36). The QTs are defined by an integral of the nuclear probability density, Eq. (19), which yields:

$$\rho_c = \frac{1}{2}(1 + \text{erf}(y_t)) + \frac{\lambda^2}{2}(\text{erf}(y_t - q_t) - \text{erf}(y_t)). \quad (40)$$

The velocities of the QTs are then:

$$\dot{y}_t = \frac{\dot{q}_t}{1 + \eta\sigma} = \frac{\bar{p}_t}{M(1 + \eta\sigma)}, \quad (41)$$

where σ denotes the probability density ratio of the BH nuclear wavepackets,

$$\sigma := \frac{\exp(-y_t^2)}{\exp(-(y_t - q_t)^2)}. \quad (42)$$

The XF coefficient C_1 is known up to a phase,

$$C_1(y, t) = \frac{\sqrt{1 - \lambda^2} e^{-y^2/2 + i\theta_1(y, t)}}{((1 - \lambda^2)e^{-y^2} + \lambda^2 e^{-(y - q_t)^2})^{1/2}}, \quad (43)$$

which is not needed for the time-derivatives of $|C_1|$. Using $\dot{q}_t = \bar{p}_t/M$, the Eulerian EOM for $|C_1|$ is

$$\frac{\partial |C_1|}{\partial t} = \frac{\bar{p}_t}{M} \frac{\sqrt{\eta\sigma}}{(1 + \eta\sigma)^{3/2}} (q_t - y). \quad (44)$$

In the moving QT frame defined by \dot{y}_t of Eq. (41), the time-dependence of $|C_1|$ is defined by the following equation:

$$\frac{d|C_1|}{dt} = \frac{\bar{p}_t}{M} \frac{\sqrt{\eta\sigma}}{(1 + \eta\sigma)^{3/2}} \left(\frac{\eta\sigma}{1 + \eta\sigma} q_t - y_t \right). \quad (45)$$

Substitution of y_m (Eq. (38)) into Eq. (44) gives

$$\left. \frac{\partial |C_1|}{\partial t} \right|_{y=y_m} = \frac{\bar{p}_t q_t}{\sqrt{32} M} - \frac{\bar{p}_t \ln(\eta)}{\sqrt{32} M q_t}, \quad (46)$$

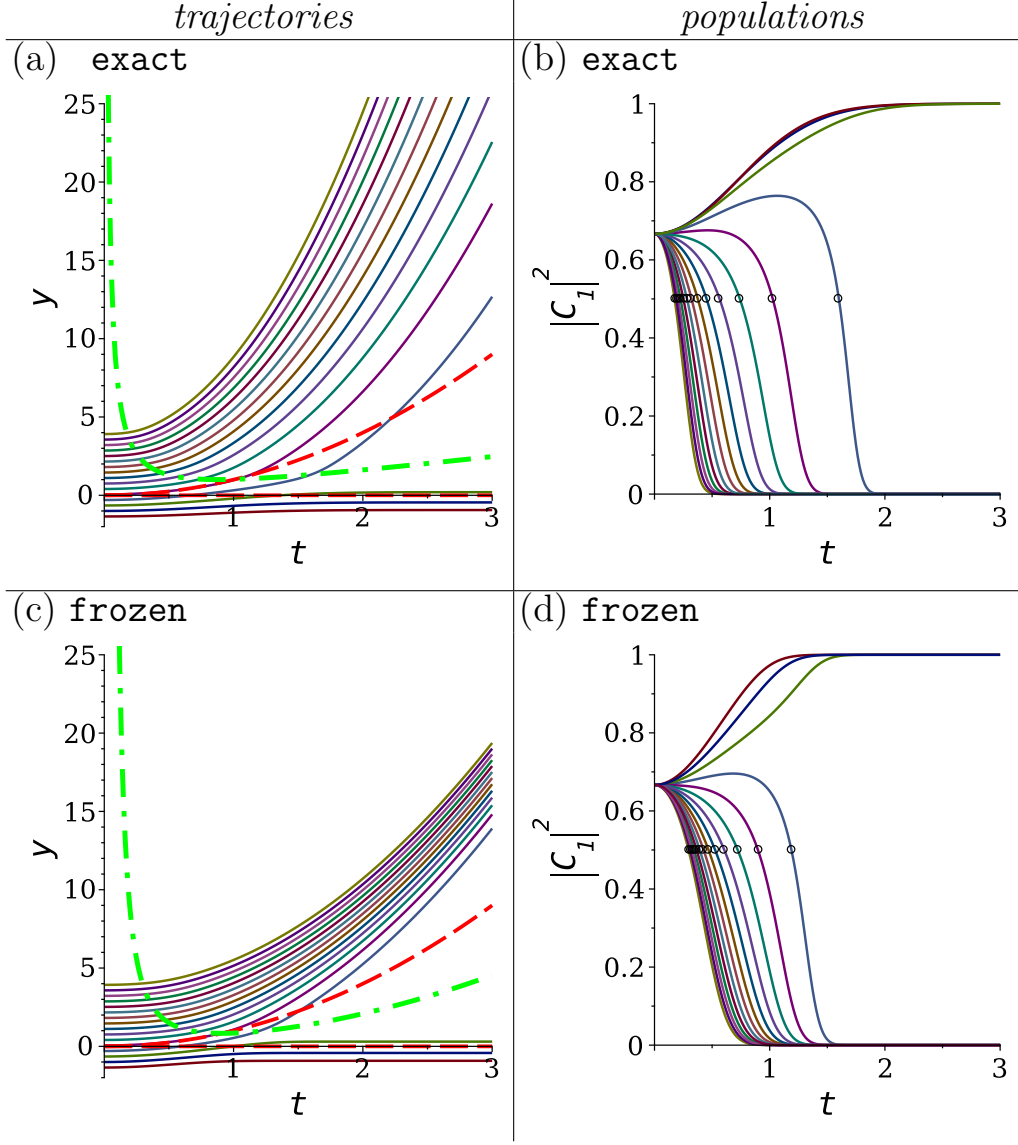


FIG. 2. The quantum trajectories and associated electronic populations for the photodissociation model. Panels (a) and (c) show the QTs (solid lines, Eq. (19)) for the exact and frozen wavepackets, respectively. The red dashed lines are the centers of the ground and excited state Gaussians (note the ground state center remains at zero for all time). The green dot dash line marks the position of equal density, $y_m(t)$. Panels (b) and (d) show the populations of the electronic ground state along each trajectory, with the colors of the solid lines corresponding to trajectories plotted in (a) and (c) correspondingly. The black open circles indicate the point where the dissociating trajectories cross $y_m(t)$.

while in the QT frame Eq. (45) yields:

$$\frac{d|C_1|}{dt} \bigg|_{y_t=y_m} = -\frac{\bar{p}_t \ln(\eta)}{\sqrt{32} M q_t}. \quad (47)$$

In Eqs (46) and (47) the term $\sim 1/q_t$ goes to zero for large q_t (long times), and for $\eta = 1$ the latter is equal to zero at all times.

Formally, the behavior of the time-derivatives of $|C_1(y, t)|$ are defined by the differential operators $(\hat{D}_1 + \hat{D}_2)C_1$ in Eq. (35). Thus, if $d|C_1|/dt$ in the QT framework is small, then we could expect the combined action of the derivatives in the RHS of Eq. (35) to be well-behaved numerically despite the step-function character of $|C_1(y, t)|$ at long times. To analyze this numerical aspect we examine the extrema of Eqs (44) and (45) by employing the following approximation: noting that the exponential dependence on y_t in σ is larger than the linear dependence of other terms, these two equations are differentiated with respect to σ and the result is solved for σ . With that the positions of the extrema, denoted y_δ , satisfy the following conditions at $y = y_\delta$ or $y_t = y_\delta$ for the Euler and Lagrange frames, respectively:

$$\sigma_{Euler} = \frac{1}{2\eta} \quad (48)$$

$$\sigma_{Lagrange} = \frac{y_\delta + 3q_t - \sqrt{9q_t^2 - 2q_t y_\delta + 9y_\delta^2}}{4(q_t - y_\delta)\eta}. \quad (49)$$

As demonstrated in Fig. 4, the extrema occur close to y_m . Thus, we represent y_δ through its displacement, δ , from y_m ,

$$y_\delta = y_m + \delta, \quad (50)$$

and solve Eqs (48) and (49) for δ taking the natural logarithm of the equations (Taylor-expanding to the first order in δ at $\delta = 0$ and in $1/q_t$ at $q_t = \infty$ in the later case). This yields the following analytic estimates for the positions of the extrema in the Euler and Lagrange frames of reference, respectively:

$$\delta_{Euler} = \frac{\ln(2)}{2q_t} \quad (51)$$

$$\delta_{Lagrange} = -\frac{1}{2q_t} \ln \left(\frac{7}{4} \pm \frac{\sqrt{41}}{4} \right) + O(q_t^{-3}). \quad (52)$$

Note that the Lagrangian solution has two solutions corresponding to the extrema to the left and right of y_m seen in Fig. 4. In both frames the extrema positions converge to y_m as $q_t \rightarrow \infty$. The analytic expressions for both frames converge as $O(q_t^{-3})$ to the numerically exact solutions shown in Fig. 3. The extremal values of the time-derivatives of $|C_1|$ are:

$$\frac{\partial|C_1(y_\delta)|}{\partial t} = \frac{\sqrt{3}\bar{p}_t q_t}{9M} + O(q_t^{-1}) \quad (53)$$

$$\frac{d|C_1(y_\delta)|}{dt} = \pm \frac{2(\sqrt{41} \pm 3)\sqrt{7 \pm \sqrt{41}}\bar{p}_t q_t}{M(11 \pm \sqrt{41})^{\frac{5}{2}}} + O(q_t^{-1}) \quad (54)$$

Disappointingly, the amplitude of the derivative extrema in *both* frames grows with time as $q_t \bar{p}_t$, which for this model means as $t^3 \propto q_t^{\frac{3}{2}}$, which matches the behavior of the accurate numerical amplitudes displayed in Fig. 3(b). Consistent with Figs 4 and 3, the constant prefactor in front of the Lagrangian extrema is smaller (by a factor of 0.6 in our model), which may slightly alleviate the numerical difficulties of applying the derivative operators $\hat{D}_1 + \hat{D}_2$ to the XF coefficients at long times (or more generally for large $q_t \bar{p}_t$).

To check if the nearly singular derivatives associated with the XF coefficients discussed above are specific to the BO eigenstate representation of the electronic wavefunction we also

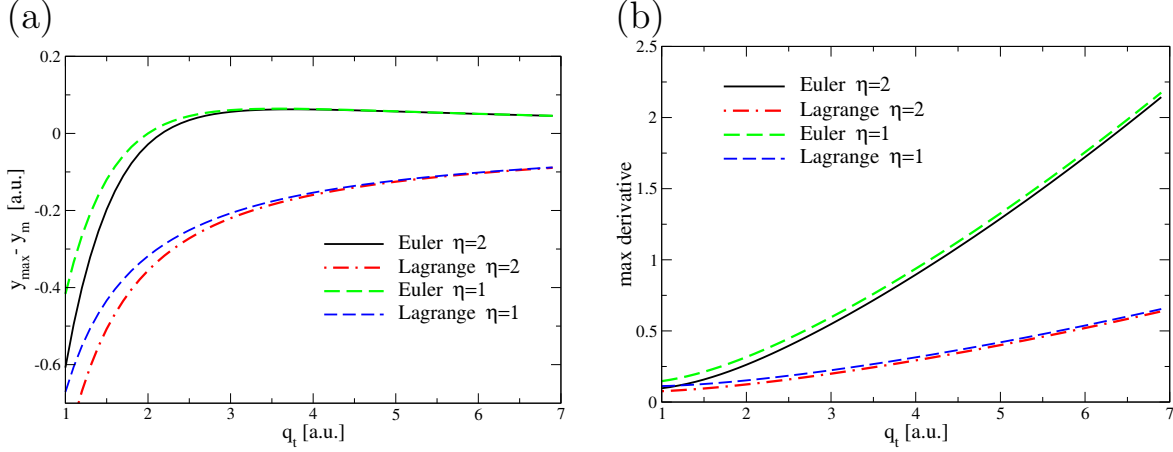


FIG. 3. The maximum time-derivative of $|C_1|$ in the Eulerian and Lagrangian frames of reference computed for $\eta = 1$ and $\eta = 2$ using $M = 100$ and $k = 20$ a.u. (a) Position with respect to the median, $y_{max} - y_m$, and (b) the largest amplitude of the extrema of the time-derivative, $\partial|C_1|/\partial t$ and of $d|C_1|/dt$ as functions of q_t for the Eulerian and Lagrangian frames of reference, respectively.

considered representation of the molecular wavefunction in a localized, or "atomic orbital", basis, $\{\chi_L, \chi_R\}$,

$$\Phi(x, y, y) := C_L(y, t)\chi_L(x, y) + C_R(y, t)\chi_R(x, y). \quad (55)$$

The subscripts L and R refer the functions associated with the left and right 'atoms', and $\chi_{R(L)}$ are the atomic orbitals. Assuming that the atomic orbitals are orthogonal, we represent the BH wavefunctions as $\chi_R \pm \chi_L$, and obtain a similar to Eqs (26) factorization: $|\psi|^2 = |\psi_L|^2 + |\psi_R|^2$, $|C_{R(L)}|^2 = |\psi_{R(L)}|^2/|\psi|^2$. The initial conditions are the same as in Table II. Initial ψ_L and ψ_R are obtained from the unitary transformation (45° rotation) of ψ_1 and ψ_2 which are used to obtain C_L and C_R . The density snapshots, obtained numerically, are shown in Fig. 5 for $t = [0, 0.64, 1.28, 1.92, 2.56, 3.20]$ a.u. The XF nuclear density and the BH ground state density, $|\psi_1|^2$ in the molecular basis are shown as black and red solid lines. The atomic basis amplitudes, $|C_L|^2$ and $|C_R|^2$ are shown as green and blue dashes. For $t > 0$ the amplitudes $|C_L|^2$ and $|C_R|^2$ exhibit an interference pattern which becomes localized at the median point rather than the step in the XF amplitudes, $|C_1|^2$ and $|C_2|^2$, for the original BH state basis. As the separation increases, the frequency of these oscillations increase in both time and space suggesting that the numerical challenges will persist in the atomic basis as well, and are inherent to the XF representation if the dynamics is characterized by the diverging wavepackets.

IV. CONCLUSIONS

In this paper we proposed a simple analytical model to study the numerical challenges associated with XF of molecular wavefunctions. The model describes the dynamics on the ground and excited electronic states as two diverging, non-interacting nuclear Gaussians. The Gaussian shapes are changing much slower than their separation, which allows for the simplified treatment of moving (i.e. centers and phases depend on time) frozen (i.e. the width parameters are constant) Gaussians.

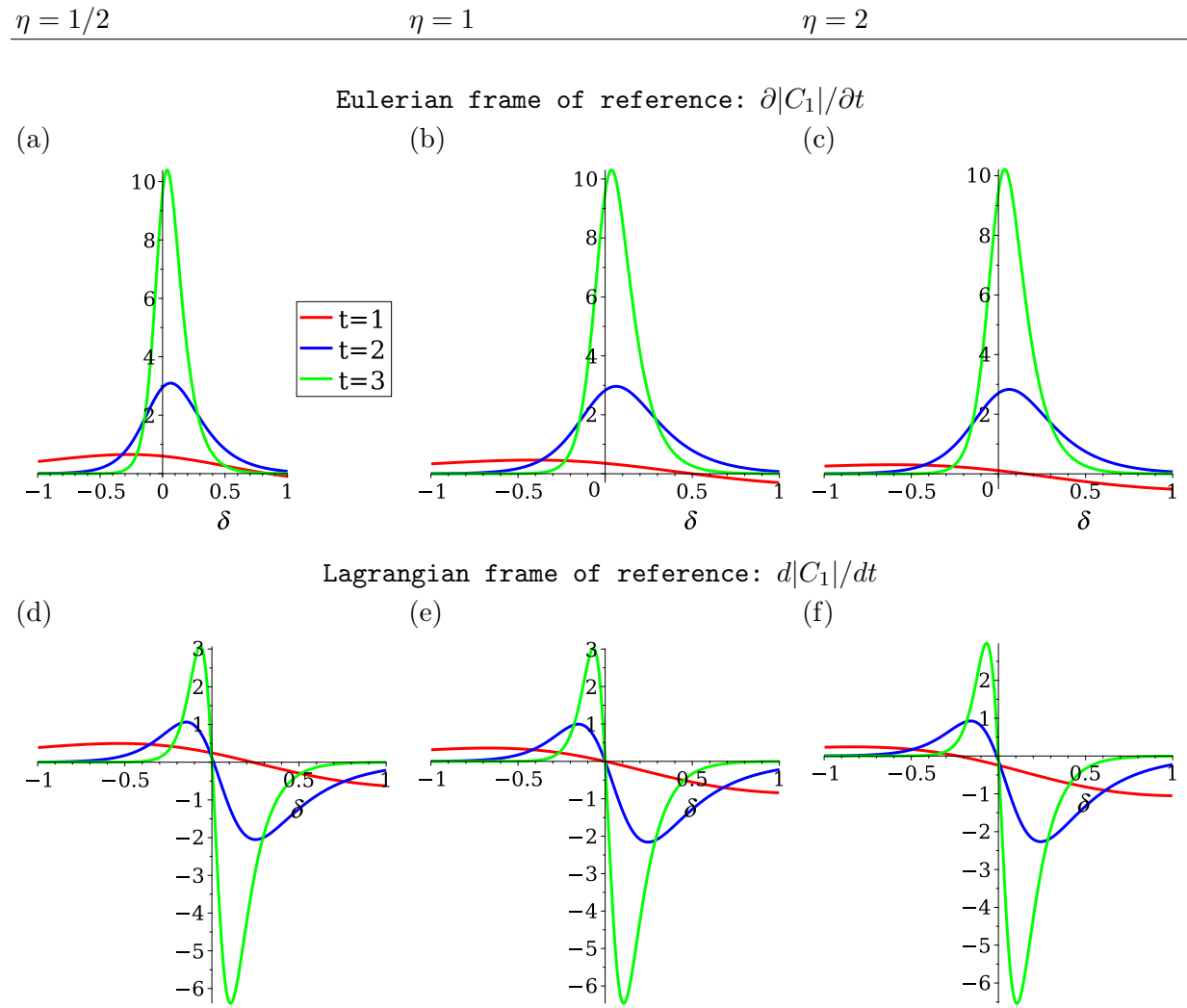


FIG. 4. Time-derivative of the ground state coefficient amplitude in (a-c) the stationary Eulerian and (d-f) moving Lagrangian frames with δ indicating the relative position to the median point. For the moving frame, in the $\eta = 1$ case, the point of 0 amplitude change is always at the median; otherwise its relative position changes. The size of the derivatives increases as $q_t \bar{p}_t$, or cubically in time as given by Eqs (44) and (45).

Within the XF representation, the electronic expansion coefficients, which describe the contributions of different electronic configuration to the overall wavefunction at each nuclear coordinate, exhibit strong non-local effects, i.e. large spatial derivatives. Their gradients approach delta functions as $t \rightarrow \infty$, and this singular behavior is present in both – the localized (atomic) and molecular – representations of the electronic coefficients. More surprisingly, the singularity remains in the moving Lagrangian frame of the quantum trajectories, although it has a smaller prefactor compared to the stationary Eulerian frame of representing the wavefunction. Based on this analysis (and also on the examination of QT dynamics for one- and two-state cases discussed in Appendix A), one solution is to switch to the state-specific trajectory descriptions once the nuclear wavepackets diverge when, e.g. they reach distinct reaction channels on the Born-Huang electronic states. We expect, that the ana-

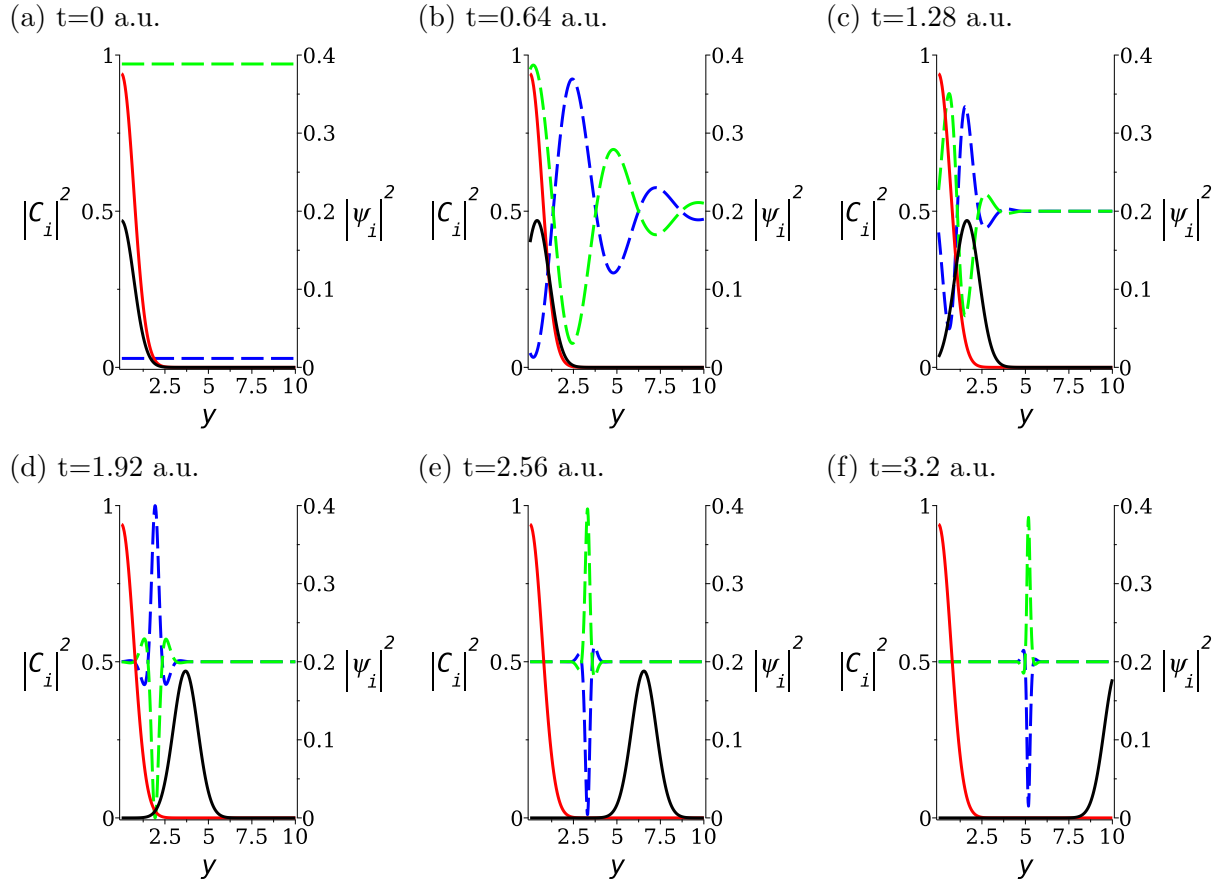


FIG. 5. XF coefficient amplitudes $|C_i|^2$ for $i = \{L, R\}$ as green and blue dashed lines. The Born-Huang ground and excited state wavepackets are shown as red and black solid lines respectively. Snapshots of the nuclear density at different separations and the corresponding electronic coefficients in the atomic orbital basis, Eq. (55). We see the presence of an interference pattern near the median point for FWPs. Initial conditions given in Table II.

lytic form of the singular terms identified in the model described in this work will facilitate the development of computational methodology to tackle the numerical challenges, and will help establish the limits of applicability of the XF method to the problems of non-adiabatic chemical dynamics. Finally, we also note, that the model discussed in this paper is relevant only to a discrete set of electronic states, thus the conclusions above are limited to this case. The XF dynamics in the regime of electronic wavepackets may be better behaved, and we intend to study this issue in the future.

ACKNOWLEDGEMENT

This material is based upon work supported by the National Science Foundation of U.S.A. under Grant No. CHE-2308922.

- [1] J.C. Tully, *Chemical dynamics at metal surfaces*, Annu. Rev. Phys. Chem. 51 (2000), pp. 153–178.
- [2] N. Shenvi, S. Roy, and J.C. Tully, *Nonadiabatic dynamics at metal surfaces: Independent-electron surface hopping*, J. Chem. Phys. 130 (2009), p. 174107.
- [3] C. Franchini, M. Reticcioli, M. Setvin, and U. Diebold, *Polarons in materials*, Nat. Rev. Mater. 6 (2021), pp. 560–586.
- [4] J.M. Frost, L.D. Whalley, and A. Walsh, *Slow cooling of hot polarons in halide perovskite solar cells*, ACS Energy Lett. 2 (2017), pp. 2647–2652.
- [5] B. Xiang and W. Xiong, *Molecular polaritons for chemistry, photonics and quantum technologies*, Chem. Rev. 124 (2024), pp. 2512–2552.
- [6] A. Abedi, N.T. Maitra, and E. Gross, *Exact factorization of the time-dependent electron–nuclear wave function*, Phys. Rev. Lett. 105 (2010), p. 123002.
- [7] R. Martinazzo and I. Burghardt, *Quantum dynamics with electronic friction*, Phys. Rev. Lett. 128 (2022), p. 206002.
- [8] S. Garashchuk, J. Stetzler, and V. Rassolov, *Factorized electron–nuclear dynamics with an effective complex potential*, J. Chem. Theory Comput. 19 (2023), pp. 1393–1408.
- [9] N.M. Hoffman, H. Appel, A. Rubio, and N.T. Maitra, *Light-matter interactions via the exact factorization approach*, Eur. Phys. J. B 91 (2018), p. 14.
- [10] A. Abedi, E. Khosravi, and I.V. Tokatly, *Shedding light on correlated electron–photon states using the exact factorization*, Eur. Phys. J. B 91 (2018), p. 12.
- [11] E. Sangiogo Gil, D. Lauvergnat, and F. Agostini, *Exact factorization of the photon–electron–nuclear wavefunction: Formulation and coupled-trajectory dynamics*, J. Chem. Phys. 161 (2024), p. 084112.
- [12] S.K. Min, F. Agostini, and E.K.U. Gross, *Coupled-trajectory quantum-classical approach to electronic decoherence in nonadiabatic processes*, Phys. Rev. Lett. 115 (2015), p. 073001.
- [13] D. Han and A.V. Akimov, *Nonadiabatic dynamics with exact factorization: Implementation and assessment*, J. Chem. Theory Comput. 20 (2024), pp. 5022–5042.
- [14] L. Dupuy, A. Rikus, and N.T. Maitra, *Exact-factorization-based surface hopping without velocity adjustment*, J. Phys. Chem. Lett. 15 (2024), pp. 2643–2649.
- [15] Y. Suzuki, A. Abedi, N.T. Maitra, and E.K.U. Gross, *Laser-induced electron localization in H_2^+ : Mixed quantum-classical dynamics based on the exact time-dependent potential energy surface*, Phys. Chem. Chem. Phys. 17 (2015), pp. 29271–29280.
- [16] A. Abedi, N.T. Maitra, and E.K.U. Gross, *Correlated electron–nuclear dynamics: Exact factorization of the molecular wavefunction*, J. Chem. Phys. 137 (2012).
- [17] S. Shin and H. Metiu, *Nonadiabatic effects on the charge transfer rate constant: A numerical study of a simple model system*, J. Chem. Phys. 102 (1995), pp. 9285–9295.
- [18] F.G. Eich and F. Agostini, *The adiabatic limit of the exact factorization of the electron–nuclear wave function*, J. Chem. Phys. 145 (2016).

[19] F. Agostini and E.K.U. Gross, *Exact factorization of the electron–nuclear wave function: Theory and applications*, in *Quantum Chemistry and Dynamics of Excited States*, chap. 17, John Wiley I& Sons, Ltd (2020), pp. 531–562.

[20] F. Agostini and B.F.E. Curchod, *When the exact factorization meets conical intersections...*, Eur. Phys. J. B 91 (2018), p. 11.

[21] A. Abedi, F. Agostini, Y. Suzuki, and E.K.U. Gross, *Dynamical steps that bridge piecewise adiabatic shapes in the exact time-dependent potential energy surface*, Phys. Rev. Lett. 110 (2013), p. 263001.

[22] B.F.E. Curchod, F. Agostini, and I. Tavernelli, *CT-MQC - a coupled-trajectory mixed quantum/classical method including nonadiabatic quantum coherence effects*, Eur. Phys. J. B 91 (2018), p. 12.

[23] S.K. Min, F. Agostini, I. Tavernelli, and E.K.U. Gross, *Ab initio nonadiabatic dynamics with coupled trajectories: A rigorous approach to quantum (de)coherence*, J. Phys. Chem. Lett 8 (2017), pp. 3048–3055.

[24] L.M. Ibele, E. Sangiogo Gil, E.V. Arribas, and F. Agostini, *Simulations of photoinduced processes with the exact factorization: State of the art and perspectives*, Phys. Chem. Chem. Phys. 26 (2024), pp. 26693–26718.

[25] E. Lorin, *Numerical analysis of the exact factorization of molecular time-dependent Schrödinger wavefunctions*, Commun. Nonlinear Sci. Numer. Simul. 95 (2021), p. 105627.

[26] G.H. Gossel, L. Lacombe, and N.T. Maitra, *On the numerical solution of the exact factorization equations*, J. Chem. Phys. 150 (2019), p. 154112.

[27] D. Bohm, *A suggested interpretation of the quantum theory in terms of "hidden" variables, I and II*, Phys. Rev. 85 (1952), pp. 166–193.

[28] R.E. Wyatt, *Quantum dynamics with trajectories: Introduction to quantum hydrodynamics*, Springer-Verlag, 2005.

[29] S. Garashchuk, V. Rassolov, and O. Prezhdo, *Semiclassical Bohmian dynamics*, in *Reviews in Computational Chemistry*, chap. 6, John Wiley & Sons, Ltd (2010), pp. 287–368.

[30] L. Cruz-Rodríguez, L. Uranga-Piña, A. Martínez-Mesa, and C. Meier, *Interacting trajectory representation of quantum dynamics: Influence of boundary conditions on the tunneling decay of resonant states*, J. Phys. B 56 (2023).

[31] L. Dupuy, G. Parlant, B. Poirier, and Y. Scribano, *Direct and accurate calculation of dwell times and time delays using quantum trajectories*, Phys. Lett. A 456 (2022), p. 128548.

[32] R. Lombardini and B. Poirier, *Interacting quantum trajectories for particles with spin 1/2*, Mol. Phys. 122 (2024), p. e2334805.

[33] A.S. Sanz and S. Miret-Artés, *A causal look into the quantum Talbot effect*, J. Chem. Phys. 126 (2007), 234106.

[34] A.S. Sanz, *Symmetries and singular behaviors with Bohmian trajectories*, J. Phys. Conf. Ser. 2883 (2024), p. 012011, Available at <https://dx.doi.org/10.1088/1742-6596/2883/1/012011>.

[35] S. Garashchuk and V.A. Rassolov, *Energy conserving approximations to the quantum potential: Dynamics with linearized quantum force*, J. Chem. Phys. 120 (2004), pp. 1181–1190.

[36] O.V. Prezhdo, *Quantized Hamilton dynamics*, Theor. Chem. Acta 116 (2006), pp. 206–218.

[37] B. Smith and A.V. Akimov, *Entangled trajectories Hamiltonian dynamics for treating quantum nuclear effects*, J. Chem. Phys. 148 (2018), p. 144106.

[38] C.C. Martens, *Surface hopping without momentum jumps: A quantum-trajectory-based approach to nonadiabatic dynamics*, J. Phys. Chem. A. 123 (2019), pp. 1110–1128.

- [39] D. Han, C.C. Martens, and A.V. Akimov, *Generalization of quantum-trajectory surface hopping to multiple quantum states*, *J. Chem. Theory Comput.* 21 (2025), pp. 2839–2853.
- [40] M. Dutra, S. Wickramasinghe, and S. Garashchuk, *Quantum dynamics with the quantum trajectory-guided adaptable gaussian bases*, *J. Chem. Theory Comput.* 16 (2020), pp. 18–34.
- [41] E.R. Bittner, J.B. Maddox, and I. Burghardt, *Relaxation of quantum hydrodynamic modes*, *Int. J. Quantum Chem.* 89 (2002), pp. 313–321.
- [42] B. Poirier, *Reconciling semiclassical and Bohmian mechanics. VI. Multidimensional dynamics*, *J. Chem. Phys.* 129 (2008), 084103.
- [43] S.V. Mousavi and S. Miret-Artes, *Stochastic bohmian mechanics within the schrodinger-langevin framework: A trajectory analysis of wave-packet dynamics in a fluctuative-dissipative medium*, *Eur. Phys. J. Plus* 134 (2019).
- [44] R.E. Wyatt, C.L. Lopreore, and G. Parlant, *Electronic transitions with quantum trajectories*, *J. Chem. Phys.* 114 (2001), pp. 5113–5116.
- [45] L. Dupuy, F. Talotta, F. Agostini, D. Lauvergnat, B. Poirier, and Y. Scribano, *Adiabatic and nonadiabatic dynamics with interacting quantum trajectories*, *J. Chem. Theory Comput.* 18 (2022), pp. 6447–6462.
- [46] S. Garashchuk, V.A. Rassolov, and G.C. Schatz, *Semiclassical nonadiabatic dynamics based on quantum trajectories for the O³P, ¹D)+H₂ system*, *J. Chem. Phys.* 124 (2006), p. 244307.
- [47] S. Garashchuk and V.A. Rassolov, *Semiclassical dynamics with quantum trajectories: Formulation and comparison with the semiclassical initial value representation propagator*, *J. Chem. Phys.* 118 (2003), pp. 2482–2490.
- [48] P. Schürger, Y. Lassmann, F. Agostini, and B.F.E. Curchod, *On the connection between the exact factorization and the Born–Huang representation of the molecular wavefunction*, *J. Chem. Phys.* 162 (2025), p. 196101.

Appendix A: QT dynamics on one and two electronic states

Here we demonstrate the quantum trajectory (QT) dynamics associated with one and two electronic states for the model of Section II C, somewhat modified for illustrative purposes. We present the trajectories assuming that two nuclear Gaussian wavepackets evolve on distinct uncoupled electronic states, from which an XF set of trajectories is constructed according to Eq. (19). For comparison, we also present the trajectories defined by the sum of the two Gaussian wavepackets, as if they were evolving on a single electronic state. In the former case, the XF nuclear probability density is given by

$$|\psi^{XF}|^2 = \langle \Psi | \Psi \rangle_x = |\psi_1(y, t)|^2 + |\psi_2(y, t)|^2, \quad (\text{A.1})$$

while in the latter case its counterpart is the probability density of a single nuclear wavefunction which generates the usual Bohmian trajectories,

$$|\psi^{Bohm}|^2 = |\psi_1(y, t) + \psi_2(y, t)|^2. \quad (\text{A.2})$$

Thus, the difference between the ensuing QT ensembles will come from the interference of the two wavepackets in case of the single-state dynamics. The results are presented in Fig. A.1.

First, let us consider the dynamics on two parabolic surfaces,

$$V_{11} = y^2/2, \quad V_{22} = V_{11} + 1. \quad (\text{A.3})$$

The constant in V_{22} does not affect the QT dynamics in the two-state system, and generates a relative phase between the two wavepackets in the one-state system. First, we will consider two wavepackets, $\psi_{1(2)}$, taken as coherent Gaussians given by Eq. (21). We will examine a symmetric and asymmetric initial conditions. In the *symmetric* case, the wavepackets are initially displaced from the minimum of V_i , $q_1(0) = -1$, $q_2(0) = 1$, have zero initial phase, $p_1 = p_2 = 0$, and their population coefficients, are equal, $\lambda_1 = \lambda_2 = 1/\sqrt{2}$. The resulting QTs are shown in Fig. A.1(a,b). In the *asymmetric* case, ψ_1 is an eigenstate ($q_1 = 0$, $p_1 = 0$, and ψ_2 is displaced, $q_2(0) = 1$, $p_2(0) = 0$; the population coefficients are equal to $\lambda_1 = \sqrt{3}/2$ and $\lambda_2 = 1/2$. The resulting QTs are shown in Fig. (A.1(c,d)). In all panels dashed red lines indicate $q_1(t)$ and $q_2(t)$; the blue dots and grey dashes outline the QTs corresponding to the dynamics of ψ_1 and ψ_2 as separate wavefunctions, while the black lines represent the QT ensemble underlying the evolution of XF nuclear wavefunction assuming two-electronic states (Fig. A.1(a,c)), or on a single electronic state (Fig. A.1(b,d)).

In all cases the QTs describing the individual wavepacket components are smooth trajectories that are parallel to the respective wavepacket center q_i . (In the asymmetric case the trajectories corresponding to ψ_1 are stationary.) In the two-state scenario, the QT trajectories corresponding to the XF wavefunction, are also smooth and cover nearly (exactly for the symmetric system) the same coordinate space as the QT ensembles of the individual wavepackets. In the one-state scenario, the trajectories corresponding to the full wavefunction, $\psi = \sum_i \psi_i$, travel around the nodal points at $t = \pi$ and near-nodal points at $t = \pi/2, 3\pi/2$. This singular behavior arises due to the interference term, $\langle \psi_1 | \psi_2 \rangle$, affecting the QTs in the one-state system. This suggests that for a one-state dynamics, 'regularized' or approximate QT ensemble could be constructed from the trajectory weight and positions only (ignoring the phase information). Such an ensemble can be used to define an efficient time-dependent basis, tailored to the evolving wavefunction, for solving the time-dependent Schrödinger equation in many dimensions.

Next, let us consider dynamics of the type discussed in Section III with V_{22} replaced by a linear ramp, $V_{22} = -ky$, $k = 2$ a.u. The initial nuclear wavepackets are identical: $a_i = 1$, $q_i = -1$, $p_i = 0$ a.u. The ground state wavepacket, ψ_1 , is a coherent Gaussian whose center oscillates as in the previous example, while the center of the second wavepacket, ψ_2 , moves downhill and spreads in space according to Eqs (23-25). The quantum, or Bohmian, trajectories, associated with the motion of the individual wavepackets are shown in Fig. A.2(a) as families of green dashes and blue dotted lines, respectively. Red dot-dashes highlight the motion of the Gaussian centers, $q_i(t)$. The QTs describing the XF wavefunction of Eq. (A.1), shown as black lines, represent a 'union' of the two sets, except that for the same uniform sampling of the trajectories (used to generate all trajectory ensembles) there are no XF trajectories in the region of the divergence of ψ_1 and ψ_2 . Fig. A.2(b) illustrates the divergent region on a smaller scale; the corresponding gradients of the XF expansion amplitude, $\nabla_y |C_1(y, t)|$ approaches the δ -function as seen in Fig. A.2(c). This behavior is the source of the numerical challenges in implementing XF in the regime of divergent nuclear wavefunction components. Thus, we argue that for practical reasons, in this regime the dynamics of the nuclear components should be 'uncoupled'. We note however, that our analysis is limited to a discrete spectrum of the electronic states, and does not extend to the dynamics involving electronic wavepackets composed of large number of the electronic states. The type of singularity discussed above may be mitigated or avoided altogether in the limit of the electronic wavepackets.

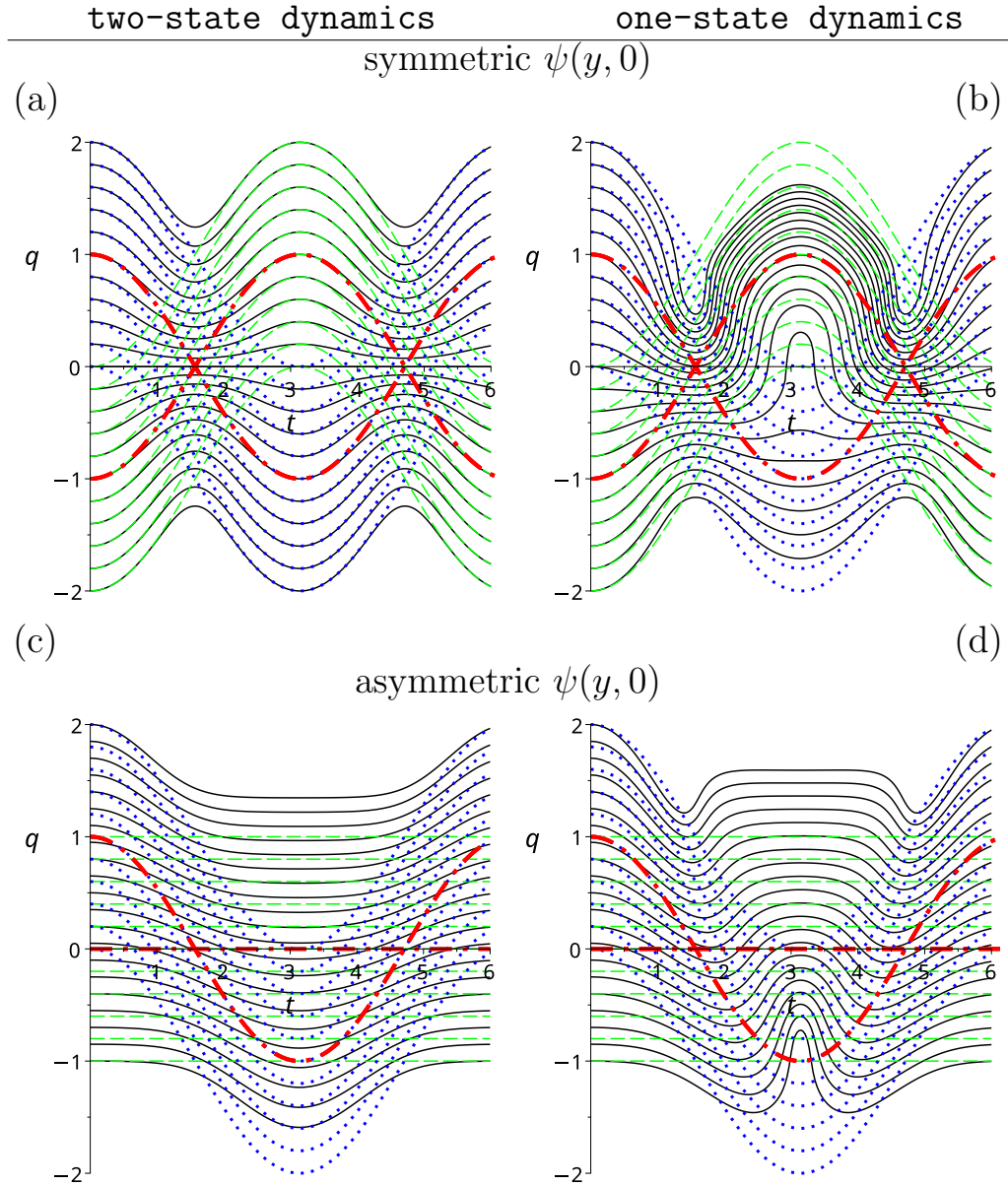


FIG. A.1. Dynamics of two coherent wavepackets. Black lines represent positions of the QT trajectories corresponding to the dynamics of ψ on two (panels (a) and (c)) and one (panels (b) and (d)) electronic states, respectively. The QT ensembles for $\psi_1(\psi_2)$ are shown as green dashed/blue dotted lines. The evolution of the GWP centers $q_{1(2)}$ is indicated as red dot-dashes.

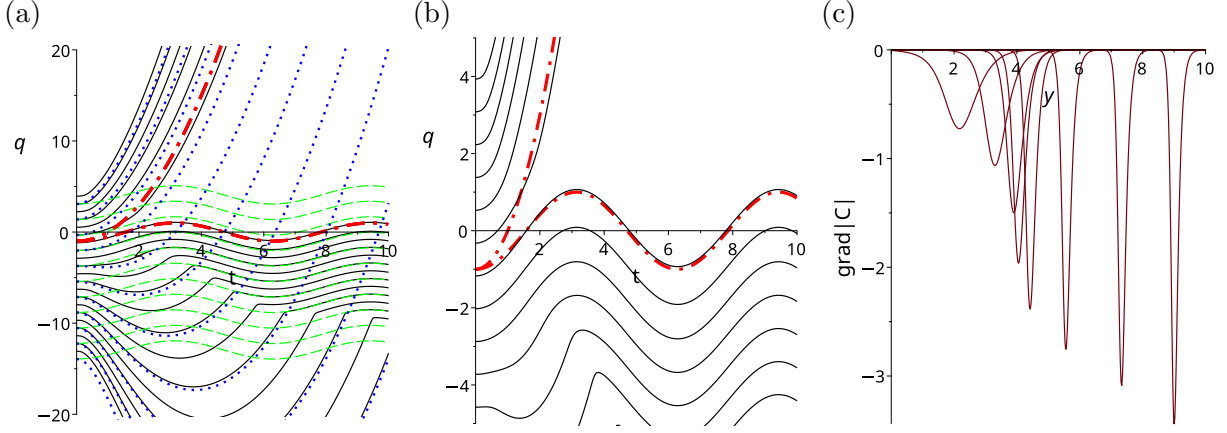


FIG. A.2. Two-state dynamics in the parabolic/linear ramp potentials. The parameters and initial conditions are $\lambda_1 = \sqrt{3}/2$, $\lambda_2 = 1/2$, $a = 1$, $q_1(0) = q_2(0) = -1$, $p_1(0) = p_2(0) = 0$. (a) The QTs of ψ_1 and ψ_2 are represented as green dashes and blue dots, respectively. The QTs of the XF wavefunction, ψ^{XF} , are displayed as black lines; red dot-dashes represent the centers of $q_{1(2)}$ as functions of time, t . The divergent region of the XF and wavepacket center trajectories is magnified in panel (b). (c) The snapshots of the gradient of the XF amplitude, $\nabla_y|C_1(y, t)|$ for $t = \{2, 3, 4, 5, 6, 7, 8, 9\}$ a.u.; the peak amplitudes increase with time, as $\nabla_y|C_1(y, t)|$ approaches the δ -function.